



# Geopositioning precision analysis of multiple image triangulation using LROC NAC lunar images



Bin Liu<sup>a,b</sup>, Mengna Jia<sup>a,c</sup>, Kaichang Di<sup>a,\*</sup>, Jürgen Oberst<sup>b,d,e</sup>, Bin Xu<sup>a</sup>, Wenhui Wan<sup>a</sup>

<sup>a</sup> State Key Laboratory of Remote Sensing Science, Institute of Remote Sensing and Digital Earth, Chinese Academy of Sciences, 100101 Beijing, China

<sup>b</sup> Technical University of Berlin, Straße des 17. Juni 135, 10623 Berlin, China

<sup>c</sup> University of Chinese Academy of Sciences, 100049 Beijing, China

<sup>d</sup> DLR Institute of Planetary Research, Rutherfordstr. 2, 12489 Berlin, Germany

<sup>e</sup> Moscow State University for Geodesy and Cartography (MIIGAiK), 105064 Moscow, Russia

## ARTICLE INFO

### Keywords:

Lunar  
Geopositioning  
Triangulation  
Multiple images  
LROC NAC image

## ABSTRACT

With continuing data acquisition from lunar orbiters, many areas of the lunar surface have been observed multiple times under different viewing conditions. This raises an issue regarding how to select the best stereo sets and achieve the highest 3D geopositioning precision in such areas. This paper presents a comprehensive analysis of the geopositioning precision of multiple image triangulation using Lunar Reconnaissance Orbiter Camera (LROC) Narrow Angle Camera (NAC) images. Seven and nine LROC NAC images are used, respectively, for the Apollo-11 and Chang'e-3 landing sites. The photogrammetric methods are developed based on a rigorous camera sensor model and rational polynomial model. Experiments with different combinations of dual images are performed for comparisons at both sites. The results demonstrate that the geopositioning precision, especially the height precision, is improved as the convergence angle increases from near 0°–50°. More importantly, we find that as the convergence angle of a stereo pair increases, the image matching precision decreases approximately linearly, which makes the geopositioning less precise. We also find that the shadow-tip distance and the aspect ratio have roughly linear effect on degrading matching quality. So these two factors also need to be considered when selecting image pairs for stereo mapping. The geopositioning precision is mainly controlled by the convergence angle when it is less than about 10° while the image matching error plays a more critical role when the convergence angle is greater than 10°. Experiments with multiple images indicate that utilizing more images produces higher precision than almost all dual-image models; meanwhile, using fewer images can produce better precision than using all available images together. A progressive selection method is proposed to find the best image combination for maximum precision and effectiveness.

## 1. Introduction

The Lunar Reconnaissance Orbiter (LRO) was launched on June 18, 2009, and entered lunar orbit on June 23, 2009. With seven science instruments, it has been a very successful mission through its seven years in orbit, including a one-year Exploration Mission, a two-year Science Mission and an extended Science Mission, currently ongoing (Keller et al., 2016). The Lunar Reconnaissance Orbiter Camera (LROC) system, one of the major instruments onboard LRO, consists of a Wide Angle Camera (WAC) and two identical Narrow Angle Cameras (NACs). The LROC NACs provide panchromatic images of the lunar surface with a pixel scale of 0.50 m from a 50 km altitude (Robinson et al., 2010). Although the LROC is not designed with built-in stereo capability, NAC

stereo images can be acquired from adjacent orbits using off-nadir slew for production of detailed and accurate Digital Terrain Models (DTMs) and orthophotos (Kirk et al., 2012). NAC images and their mapping products have been widely used to support various scientific investigations, e.g., landing site topographic analysis (Haase et al., 2012; Karachvtseva et al., 2013; Wu et al., 2014; Clegg-Watkins et al., 2016), lunar regolith thickness surveying (Bart et al., 2011; Di et al., 2016b), and geopositioning of anthropogenic features (Liu et al., 2015a b; Wagner et al., 2017).

Photogrammetric processing of LROC NAC images has been performed by several teams, e.g., Arizona State University (ASU), German Aerospace Center (DLR), Technische Universität Berlin (TUB), National Aeronautics and Space Administration (NASA) Ames Research Center,

\* Corresponding author.

E-mail address: [dikc@radi.ac.cn](mailto:dikc@radi.ac.cn) (K. Di).

University of Arizona (UA), Ohio State University (OSU), and United States Geological Survey (USGS), making use of ISIS and SOCET SET, as well as other in-house developed software packages. Through bundle adjustment of stereo images, the root mean square (RMS) errors can be reduced to sub-pixel to one pixel level (Henriksen et al., 2017). With continued data acquisition from LROC NACs, many high priority science and exploration targets have been observed multiple times with different slew angles (typically  $\leq 30^\circ$ ) (Henriksen et al., 2016). How to identify the best stereo sets and achieve the best geopositioning precision with multi-image coverage becomes an important issue. For choosing a NAC stereo pair, uniform illumination condition, image overlap, similar spatial resolution, convergence angle, and compatible spectral wavelength range were empirically considered in previous investigations (Becker et al., 2015; Henriksen et al., 2016, 2017). In the study of dual-sensor stereo geometry of Ikonos-QuickBird stereo pairs for Earth observation, Jeong and Kim (2014) considered the bisector elevation and asymmetry angle, in addition to the convergence angle. The geometry strength and the image matching condition have also been considered as two main factors, which affect geopositioning precision in previous studies. However, image matching conditions are usually evaluated qualitatively, and the relationship between image matching error and stereo geometry strength (depicted by the convergence angle) has not been investigated. Meanwhile, stereo mapping with NAC images has typically been processed with dual images. Recently, triangulation with three or more NAC images was analyzed in the Chang'e-3 (CE-3) landing site in a recent preliminary study (Di et al., 2016a).

In this paper, we perform a comprehensive quantitative analysis of multi-image triangulation using LROC NAC images with consideration of both convergence angle and image matching error. First, all combinations of dual-image triangulation are performed at both Apollo-11 and CE-3 landing sites to evaluate the relationships among geopositioning precision, convergence, and image matching error. Then, an in-depth analysis is performed based on numerical simulation and theoretical deduction. Next, triple or more NAC image triangulation is carried out using a progressive method with one image added to the existing optimal combination each time. Our study demonstrates the advantage of triangulation using multiple images in LROC NAC photogrammetry, reveals the relationships among geopositioning precision, convergence, and image matching error, and presents an effective method for selection of the best image combination to achieve the highest precision in multiple image triangulation.

## 2. Methodology

The method adopted in this research mainly includes the following steps: establishment of the rigorous sensor models as well as the rational function models of the LROC NAC images, block adjustment of multiple images based on rational function models, and geopositioning precision evaluation with different combinations of the images.

### 2.1. Rigorous sensor model (RSM)

The RSM connects the image coordinates of a LROC NAC image with the corresponding lunar body fixed coordinates. It is represented by the collinearity equations with interior and exterior orientation elements retrieved from the corresponding SPICE kernels (NAIF, 2014). The RSM can be described as (Di et al., 2014):

$$\begin{bmatrix} X - X_s \\ Y - Y_s \\ Z - Z_s \end{bmatrix} = \lambda \mathbf{R}_{ol} \mathbf{R}_{bo} \mathbf{R}_{ib} \begin{bmatrix} x \\ y \\ -f \end{bmatrix} = \lambda \mathbf{R} \begin{bmatrix} x \\ y \\ -f \end{bmatrix} \quad (1)$$

where  $(x, y)$  are the image focal plane coordinates,  $f$  is the focal length,  $(X, Y, Z)$  and  $(X_s, Y_s, Z_s)$  represent the lunar-surface-point coordinates and

the position of photography center in the lunar body-fixed coordinate system (LBF), respectively;  $\mathbf{R}_{ib}$  is the rotation matrix from the image space coordinate system to the spacecraft body coordinate system (BCS);  $\mathbf{R}_{bo}$  is the rotation matrix from the BCS to the orbit coordinate system (OCS);  $\mathbf{R}_{ol}$  is the rotation matrix from the OCS to the LBF;  $\mathbf{R}$  is the combination of these three rotation matrices and  $\lambda$  is a scale factor. The main parameters are shown in Fig. 1.

Based on collinearity equations, the 3D coordinates of a ground point can be calculated through space intersection using the image coordinates of corresponding points from a stereo image pair. Alternatively, the ground location can also be calculated from a single image if the elevation of the point is known (i.e., a Digital Terrain Model (DTM) is available). Here, we use the method to derive the latitude and longitude ( $L, B$ ) position from the image coordinates ( $row, col$ ) and the given height  $h$ . First, the image coordinates ( $row, col$ ) are transformed to  $[x, y, -f]^T$  by interior orientation as follows (NAIF, 2014):

$$xd = (col - \text{BORESIGHT\_SAMPLE}) \cdot \text{PIXEL\_PITCH} \quad (2)$$

$$r = xd \quad (3)$$

$$x = xd / (1 + k1 \cdot r^2) \quad (4)$$

where,  $\text{BORESIGHT\_SAMPLE}$  is the principal point coordinate,  $\text{PIXEL\_PITCH}$  is the pixel size of the image,  $xd$  is the distorted position (the measured position),  $k1$  is the distortion coefficient,  $r$  is the distance between the optical center and image points, and  $x$  is the corrected focal plane position in mm. These parameters of left and right cameras (NAC-L and NAC-R) used for interior orientation are listed in Table 1. The NAC cameras are line scanners (single line CCD),  $yd$  is unmeasured and probably unimportant so  $y$  is assumed to be zero in this research.

Next, the  $R[x \ y \ -f]^T$  are normalized to  $[u_1 \ u_2 \ u_3]^T$  by Eq. (5):

$$\begin{bmatrix} u_1 \\ u_2 \\ u_3 \end{bmatrix} = R \begin{bmatrix} x / \sqrt{x^2 + y^2 + f^2} \\ y / \sqrt{x^2 + y^2 + f^2} \\ -f / \sqrt{x^2 + y^2 + f^2} \end{bmatrix} \quad (5)$$

If  $R_L$  represents the lunar radius, Eq. (6) can be established from the sphere formula:

$$X^2 + Y^2 + Z^2 = (R_L + h)^2 \quad (6)$$

Substituting RSM into Eq. (6),  $\lambda$  can be acquired as below:

$$(\lambda u_1 + X_s)^2 + (\lambda u_2 + Y_s)^2 + (\lambda u_3 + Z_s)^2 = (R_L + h)^2 \quad (7)$$

$$\lambda^2 + 2(X_s u_1 + Y_s u_2 + Z_s u_3) \lambda + (X_s^2 + Y_s^2 + Z_s^2) - (R_L + h)^2 = 0 \quad (8)$$

$$\lambda = -(X_s u_1 + Y_s u_2 + Z_s u_3) \pm \sqrt{(X_s u_1 + Y_s u_2 + Z_s u_3)^2 - (X_s^2 + Y_s^2 + Z_s^2) + (R_L + h)^2} \quad (9)$$

Finally,  $(X, Y, Z)$  are obtained by substituting  $\lambda$  into RSM and the latitude and longitude ( $L, B$ ) can be calculated by Eq. (10):

$$\begin{aligned} L &= \arctan(Y/X) \\ B &= \arctan\left(\frac{Z}{\sqrt{X^2 + Y^2}}\right) \end{aligned} \quad (10)$$

### 2.2. Rational function model (RFM)

The RFM can be used to establish the relationship between image-space coordinates and object-space coordinates with the ratios of polynomials (Di et al., 2003), as shown in Eq. (11):

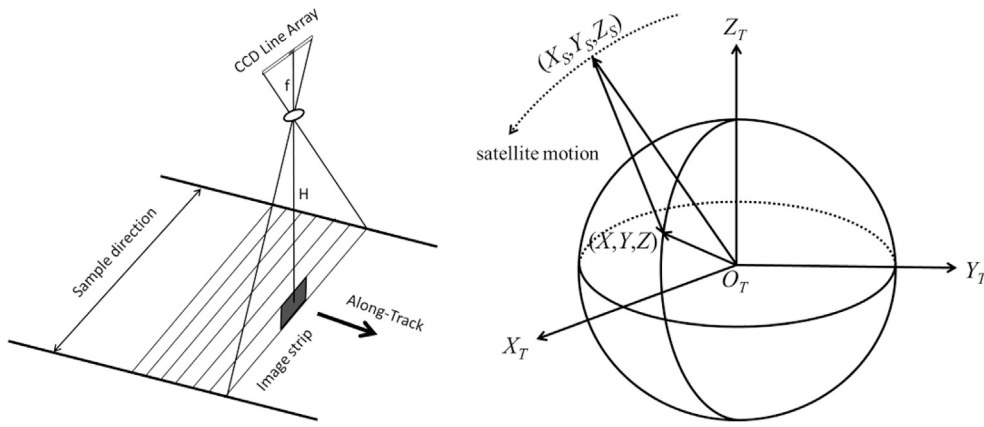


Fig. 1. The schematic diagrams of linear array push-broom imaging and RSM parameters. (Left: The schematic diagram of linear array push-broom imaging; Right: The schematic diagram of RSM parameters.  $H$  is the flight height and  $f$  is the focal length.  $O_T-X_T Y_T Z_T$  is the LBF coordinate system,  $(X, Y, Z)$  and  $(X_s, Y_s, Z_s)$  are the lunar-surface-point coordinates and the position of photography center in the LBF.).

Table 1  
Interior orientation parameters of LROC NAC imagery (NAIF, 2014).

	Left	Right
BORESIGHT_SAMPLE (pixel)	2548	2496
PIXEL_PITCH (mm)	$7.0 \times 10^{-3}$	$7.0 \times 10^{-3}$
$kI$	$1.81 \times 10^{-5}$	$1.83 \times 10^{-5}$
$f$ (mm)	699.62	701.57

$$r = \frac{P_1(X, Y, Z)}{P_2(X, Y, Z)} \quad (11)$$

$$c = \frac{P_3(X, Y, Z)}{P_4(X, Y, Z)}$$

The three-order polynomial  $P_i$  ( $i=1, 2, 3$ , and  $4$ ) has the following general form:

$$P_i(X, Y, Z) = a_1 + a_2X + a_3Y + a_4Z + a_5XY + a_6XZ + a_7YZ + a_8X^2 + a_9Y^2 + a_{10}Z^2 + a_{11}XYZ + a_{12}X^3 + a_{13}XY^2 + a_{14}XZ^2 + a_{15}X^2Y + a_{16}Y^3 + a_{17}YZ^2 + a_{18}X^2Z + a_{19}Y^2Z + a_{20}Z^3 \quad (12)$$

where  $a_1, a_2 \dots$  to  $a_{20}$  are the coefficients of the polynomial function  $P_i$ , named as the rational polynomial coefficients (RPCs).

The RPCs of each image are derived by least-squares fitting using vast numbers of virtual control points generated by the RSM of the image with the procedure described below. First, a series of grid points in a certain interval are generated in every image as the virtual control points in image space. Then, the elevation in the object space is divided into several layers and the ground coordinates of the virtual control points in every layer are calculated by the method elaborated in the previous section. Finally, the RPCs are derived by these virtual control points through least-squares fitting. It is worth mentioning that due to the descending and ascending modes, some NAC images are mirror-flipped; in order to facilitate stereo image matching, those images are corrected to normal direction and the RSM and RFM are established for the corrected images.

From the literature and our experience (Tao and Hu, 2001; Wang et al., 2005; Liu et al., 2016), we know that the RFM can approximate RSM with a precision of 1/100 pixel level in image space, even in the range of emission angles in our research (Jeong et al., 2015). That is to say, in practical applications, RFM can be used to replace RSM without loss of accuracy. Similar to RSM, RFM can be used to calculate the 3D ground position using image coordinates from a stereo pair or from a

single image with a known DTM. Compared with RSM, RFM has the advantages of simplicity and independency of sensors. It is particularly advantageous in integrated mapping using multiple images from the same orbiter or different orbiters.

### 2.3. Block adjustment based on RFM

Due to orbit and attitude errors, the RSM, as well as the fitted RFM, may not be sufficiently accurate for mapping applications. The ge positioning error can be expressed by back-projection error in image space and can be corrected through block adjustment of two or more images. For RFM-based block adjustment, instead of re-solving the RPCs, correction parameters for image coordinates (row and column) are usually incorporated. The affine transformation model (Liu et al., 2014) in image space, shown in Eq. (13), is used to realize such correction:

$$F_r = P_{r_0} + P_{r_1}c' + P_{r_2}r' + r' - r = 0$$

$$F_c = P_{c_0} + P_{c_1}c' + P_{c_2}r' + c' - c = 0 \quad (13)$$

where  $(r, c)$  are the measured (matched) image coordinates,  $(r', c')$  are the projected image coordinates of tie points calculated from ground points using RFM, and  $p_{r_0}, p_{r_1}, p_{r_2}, p_{c_0}, p_{c_1}, p_{c_2}$  are affine transformation parameters. The affine transformation parameters for each image as well as the 3D coordinates of the tie points are solved iteratively by least-squares adjustment.

### 2.4. Geopositioning precision evaluation

The geopositioning precision is evaluated by check points. Control points and check points are selected according to the NASA PDS products of Apollo-11 and CE-3 landing sites. Both DTM and Digital Orthophoto Map (DOM) are used to derive the 3D coordinates of the control and check points. Evaluating the absolute geopositioning precision is difficult in the lunar/planetary domain where ground truth is extremely limited. Using an archived DTM/DOM as “truth” may be theoretically weak to some extent. But, in general, higher resolution products usually have higher internal precision. In the condition of no absolute ground truth, it is practically feasible to use the high quality archived products as reference for geopositioning precision evaluation.

Tie points in the overlap regions are extracted by cross-correlation and least-squares matching of interest points and possible gross errors are detected and removed by a RANSAC (RANDOM Sample Consensus) algorithm. The general form of the least-squares matching used in this research is shown in Eq. (14). According to the coordinates of tie points in object space, the back projection residuals are calculated and named as the image plane errors. Then, the RMS residuals between the coordinates

calculated from block adjustments and the true values of check points are taken as the indicators of the precision in object space.

$$g_1(x, y) + n_1(x, y) = h_0 + h_1 g_2(a_0 + a_1 x + a_2 y, b_0 + b_1 x + b_2 y) + n_2(x, y) \quad (14)$$

where  $g_1$  and  $g_2$  are the grayscale values of the conjugate regions of the stereo images,  $n_1$  and  $n_2$  are the random noises,  $a_0, a_1, a_2, b_0, b_1, b_2$  are the geometric transformation parameters and  $h_0, h_1$  are parameters of the radiometric transformation between the two regions.

### 3. Experiments and analysis

#### 3.1. Data set

This investigation uses two sets of images from LROC NAC, one of which consists of seven images covering the Apollo-11 landing site, and the other includes nine images covering an area of 12 km × 75 km around the CE-3 landing site. The images were all downloaded from the LROC website (<http://lroc.sese.asu.edu>). They were chosen from dozens of available images for their less noise (judged by manual interpretation in our research), not too severe shadow, reasonable overlapping area, similar illumination condition and similar pixel scale. Since the obliquity of Moon is only about 1.5°, illumination differences come mainly from time of day effect on incidence angle (Kirk et al., 2016) rather than seasonal effect on sun azimuth as can be the case on Mars and the Earth. The biggest differences are between images obtained in the morning and afternoon, leading to opposite illumination that greatly complicates image matching. We have therefore selected only images obtained after local noon, with illumination from the west. All images were obtained after 2012, when mission operations were modified to minimize the effect of spacecraft vibrations. Distortion of the images by “jitter” is thus not a major concern in this study.

To remove systematic offsets in the stereo observations, a block adjustment was performed to account for deviations in the modeled spacecraft position and orientation. We use the existing relatively higher quality and resolution DTM and DOM as “truth” data for controlling and checking, though it's not totally reasonable. In practical applications, we advocate bundle adjustment for all DTM production, which could be controlled and evaluated by any reasonable control source (e.g., Lunar Orbiter Laser Altimeter data).

The Apollo-11 landing site images, with pixel scales from 0.98 m to 1.08 m, were obtained from January 28, 2013 to July 14, 2014. Six out of the seven images have the size of 5064 × 52224 pixels and the remaining image, M1159956344R, is 5064 × 45056 pixels. In this landing site, the DTM and DOM products, which were generated from the stereo image pair M150361817 and M150368601, are available and were downloaded from [http://wms.lroc.asu.edu/lroc/view\\_rdr/NAC\\_DTM\\_APOLLO11](http://wms.lroc.asu.edu/lroc/view_rdr/NAC_DTM_APOLLO11), used as references for precision evaluation. The pixel scales of the two original images are about 0.5 m, and the resolutions of the derived DOM and DTM are 0.5 m and 2.0 m, respectively.

The LROC NAC images of the CE-3 landing site were acquired from January 15, 2012 to January 21, 2014. The pixel scales range from 1.48 m to 1.76 m and the size of the original images are 5064 × 52224

pixels. The DTM and DOM data, which were generated from the stereo images M1144922100 and M1144936321 and have pixel scales of 1.6 m, were also downloaded ([http://wms.lroc.asu.edu/lroc/view\\_rdr/NAC\\_DTM\\_CHANGE3](http://wms.lroc.asu.edu/lroc/view_rdr/NAC_DTM_CHANGE3)) and used as references for precision evaluation.

The image names and their main parameters, such as pixel size, emission angle, incidence angle, subsolar azimuth and central location are listed in Tables 2 and 3. The layouts of the ground coverage of all images used in the study are shown in Fig. 2a and b, with the background of a LROC WAC image. The north direction and the scale bars are placed in upper-right and lower-left corners of the figures, respectively, while the yellow crosses in the center mark the landing points of Apollo-11 and CE-3. Tables of the key parameters describing each possible stereo pair are presented in the supplementary online material. These include the stereo convergence angle, the ratio of aspect ratios, and the shadow-tip distance. The shadow-tip distance, which is a quantitative measure of the mismatch in illumination conditions, is calculated by the method proposed by Becker et al. (2015). The aspect ratio is the ratio of scaled pixel width and height. The scaled pixel width is decided by the CCD size, focal length of the camera, flight height of the orbiter and slew angle. Besides, the scaled pixel height is mainly decided by the exposure time.

The main auxiliary data for the research is the nominal navigation data provided by the LRO project, given in the formats of “SPICE” kernels (the abbreviation for ‘Spacecraft ephemeris, Planet, satellite, comet or asteroid ephemerides, Instrument description kernel, C-Matrix pointing kernel and Events kernel’), which can be downloaded from [http://naif.jpl.nasa.gov/pub/naif/pds/data/lro-l-spice-6-v1.0/lrosp\\_1000](http://naif.jpl.nasa.gov/pub/naif/pds/data/lro-l-spice-6-v1.0/lrosp_1000). Using USGS ISIS software, the instrument geometric parameters, such as the interior and exterior orientation elements within the SPICE kernel, can be retrieved and attached to every NAC image. The SPICE kernel used here has been updated after precise orbit determination and on-orbit calibration, which provides an accuracy of spacecraft position of about 20 m (Mazarico et al., 2012; Humm et al., 2016; Speyerer et al., 2016).

Using the method briefly described in Section 2.4, 119 tie points showed in all seven images of the Apollo-11 landing site are obtained and the corresponding points on the DOM are acquired by least-squares matching to get the horizontal coordinates, 61 points of which are successfully matched. Seven and fifteen evenly distributed tie points are chosen as control points and check points, respectively. The vertical coordinates of these points are obtained from the corresponding DEM. The distribution of the seven ground control points (green triangles) and fifteen check points (red circles) used to evaluate the final geopositioning precision is also shown in Fig. 2a.

In the same way, 129 tie points, identified in all nine images of the CE-3 landing site, are selected and matched with the DOM to obtain the horizontal coordinates of 63 successfully matched points. Eight ground control points (green triangles) and sixteen check points (red circles), evenly distributed near the CE-3 landing site are shown in Fig. 2b.

#### 3.2. Geopositioning precision of a stereo pair

To investigate the geopositioning precision of multi-image triangulation, we first compare the precision of the dual-image combinations. 21 and 36 image pairs are combined from the seven images of the Apollo-11

**Table 2**  
Images in Apollo-11 landing area used in the experiment.

Image name	ID	Scaled pixel width (m)	Scaled pixel height (m)	Emission angle (°)	Slew angle (°)	Incidence angle (°)	Subsolar azimuth (°)	Center latitude (°)	Center longitude (°)
M1114007294R	A1	1.04	1.00	16.12	16.35	42.61	179.60	0.57	23.45
M1114014396R	A2	0.97	1.00	3.83	-2.53	43.60	179.62	0.55	23.44
M1114021499R	A3	1.11	1.00	22.43	-20.09	44.56	179.62	0.56	23.41
M1126972080L	A4	1.12	1.05	20.51	-17.70	72.36	180.19	0.77	23.41
M1126986303R	A5	1.11	1.05	20.20	17.96	74.50	179.89	0.80	23.53
M1129340193R	A6	1.05	1.05	14.26	12.37	47.53	180.92	0.68	23.52
M1159956344R	A7	0.99	1.04	4.34	3.00	46.99	180.70	0.78	23.46

**Table 3**  
Images in CE-3 landing area used in the experiment.

Image name	ID	Scaled pixel width (m)	Scaled pixel height (m)	Emission angle (°)	Slew angle (°)	Incidence angle (°)	Subsolar azimuth (°)	Center latitude (°)	Center longitude (°)
M181302794L	C1	1.59	1.55	1.79	−0.01	71.7	198.34	43.42	340.49
M183661683L	C2	1.59	1.54	1.79	−0.02	54.12	223.5	44.33	340.34
M1142554338L	C3	2.05	1.46	34.72	30.00	73.87	213.72	44.63	340.35
M1142568554L	C4	1.62	1.46	18.41	15.26	75.24	199.98	44.4	340.41
M1144922100L	C5	1.65	1.46	20.18	16.88	56.49	228.21	44.36	340.48
M1144929211L	C6	1.53	1.46	11.19	8.64	57.06	222.66	44.37	340.47
M1144936321L	C7	1.49	1.46	1.79	−0.01	57.62	218.41	44.37	340.43
M1144943432L	C8	1.52	1.46	7.96	−8.98	58.21	215.3	44.37	340.43
M1144950543L	C9	1.63	1.46	17.16	−17.42	58.78	213.31	44.37	340.40

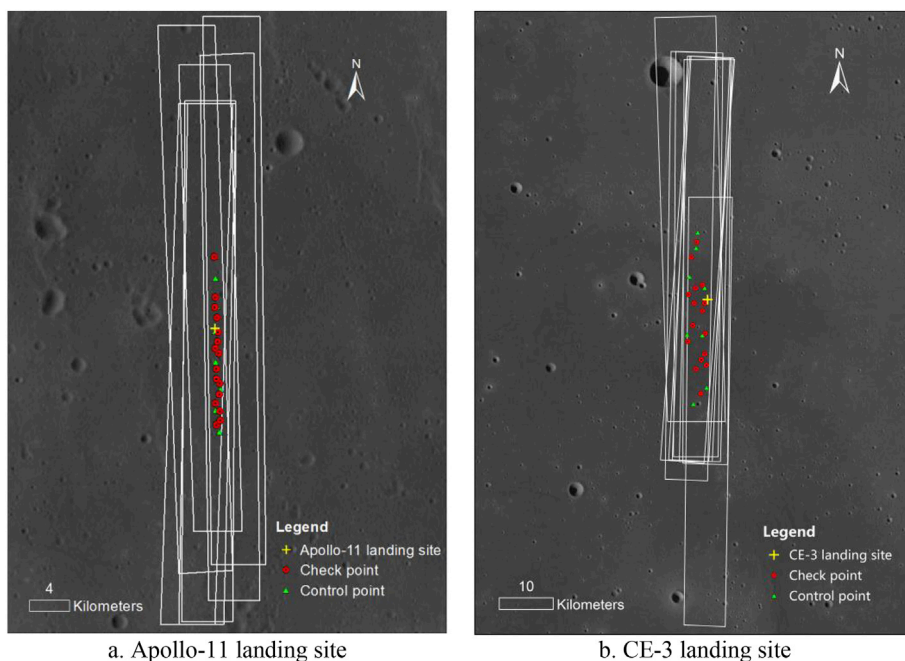


**Fig. 2.** Layouts of the ground coverage of (a) seven LROC NAC images of the Apollo-11 landing site and (b) nine LROC NAC images of the CE-3 landing site, as well as the distribution of control points and check points.

landing site and nine images of the CE-3 landing site, respectively, and the convergence angles of each pair are calculated as well as the positioning errors in object space.

For the Apollo-11 landing site, the geopositioning results of the 15 check points show that when only two images are used for 3D triangulation, the plane coordinates can reach the precision of 0.36 m–2.27 m, and the height precision is from 0.37 m to 7.22 m. The best precision from the dual-image stereo are 0.33 m, 0.14 m, and 0.37 m in along-

track, cross-track, and height directions, respectively. Similarly, for the CE-3 landing site, the dual-image planar errors of the 16 check points are between 0.54 m and 2.54 m and the height errors range from 0.71 m to 8.16 m. The smallest errors from these dual-image combinations are 0.31 m, 0.36 m, 0.71 m in along-track, cross-track and height directions, respectively.

Fig. 3 shows the relationship between the convergence angle and the positional error, and the convergence angle and the image matching

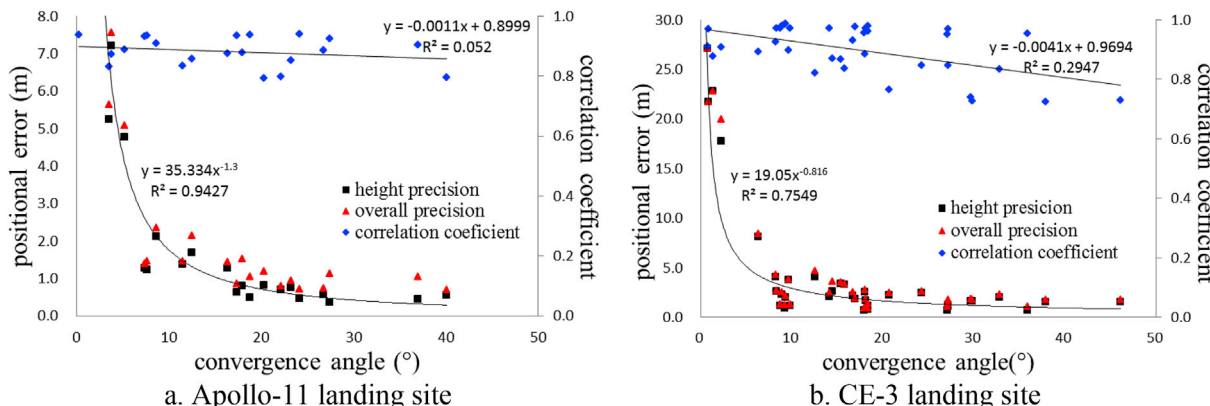


**Fig. 3.** The relationship between the convergence angle and the positional error, the convergence angle and the image correlation coefficient, for Apollo-11 (a) and CE-3 (b) landing site.

precision (depicted by mean correlation coefficient of a stereo pair from the least-squares matching results) of the check points. Here the correlation coefficient can be the indicator of image matching precision since the same window size and matching method are used for all image pairs. There is a general trend that the geopositioning precision (especially the height precision) is improved with the increase in the convergence angle of the two images in the range of our research (0°–50°). With the increase of the convergence angles, the geopositioning errors decrease as a power function, which is similar to the result of Tran et al. (2010a; 2010b). It can also be seen that when convergence angles are reduced from about 10° to 0°, the geopositioning precision decreases rapidly due to the weakening of the geometric strength of the stereo pair.

Fig. 3 also clearly shows that matching precision degrades roughly linearly with convergence angle, though the effect is weak enough that the positioning errors still decline according to a power law with an exponent near  $-1$ , as would be expected if matching precision were constant and the geometric strength of the stereo pairs were the only consideration. For both experiments, the image pairs with the largest convergence angles have relatively smaller correlation coefficients, while the pair with the second largest convergence angle for the Apollo-11 site surpasses the largest in height precision because of its high correlation coefficient, as does the pair with the third largest convergence angle for the CE-3 site. To the best of our knowledge, the influence of the convergence angle on image matching precision has never been considered previously.

In Fig. 3, it is very interesting to see that at similar convergence angles, both the positional errors and the correlation coefficients may vary significantly. We find that in these cases the higher positioning precision (lower positional errors) always corresponds to higher correlation coefficients. This indicates that not only the convergence angle but also the image matching precision plays important role in the ultimate geopositioning precision. A detailed analysis of the data of Fig. 3 reveals that when the convergence angle is smaller than about 10°, the geopositioning precision is mainly affected by the convergence angle, as the stereo calculation would be unstable under such condition; meanwhile, the image matching precision begins to dominate the error budget when the convergence angle is larger than 10°.

As a conclusion, we suggest that when selecting image pairs for 3D triangulation, both convergence angle and image matching error should be taken into consideration, especially when the convergence angles exceed a critical threshold (about 10°). There remains considerable scatter in the matching correlation results, however, so it is of interest to investigate whether other quantitative factors (some of which have been

### 3.3. Image matching precision analysis with quantitative factors

We further plot the correlation coefficient against the illumination difference as measured by shadow-tip distance in Fig. 4 and against the ratio of aspect ratios in Fig. 5. The roughly linear effects of these parameters on degrading matching quality are clear, so that they must also be considered in selection of image pairs for stereo mapping.

It is worth mentioning that the matching method is also a key point of the matching precision analysis. We used the affine transformation in least-squares matching (as shown in Eq. (14)), so the mismatch of pixel scale could be compensated for just as in methods that pre-rectify the images. However, we found that the aspect ratios of LROC NAC images are strongly related to slew angles, as we can see from Fig. 6. This is because when the CCD size, focal length of the camera and the flight height are fixed, the slew angle will be the key factor to decide the scaled pixel width. Meanwhile the slew angle has little effect on the scaled pixel height. Then big slew angles cause big aspect ratios. The degradation of correlation coefficient with respect to aspect ratio is not caused by the pixel scale mismatch, but the complex geometric distortion with the slew.

### 3.4. Numerical simulation and interpretation

To further analyze the relationship among convergence angle, image matching error, and positioning precision, a quantitative investigation is performed using a series of simulated images. It is widely accepted that the stereo convergence angle has strong impact on height errors (but little effect on horizontal errors) (Jeong and Kim, 2014). However, the best height precision in the Apollo-11 and CE-3 experiments is not achieved by the largest convergence angles, so that there should be some other influencing factors. In principle, larger observation angles may lead to more severe geometric distortion in images, making the matching between stereo images more difficult. We investigated the relationship between the convergence angle and the matching precision by simulated images generated from the existing DEM and DOM products of LROC NAC. For simulated image pairs with different convergence angles, the true image locations of the corresponding points are known; the matched locations are compared with the true locations, whose RMS differences are considered as matching errors.

The simulated images are based on DEM, the collinearity equation together with geometric parameters of LRO spacecraft and NAC instruments. First, the images are simulated to be taken at the height of the LRO average orbit with the virtual camera having a focal length and pixel size identical to that of the NAC camera. Second, the image coordinates of every pixel are set in advance and then transformed to object space by the

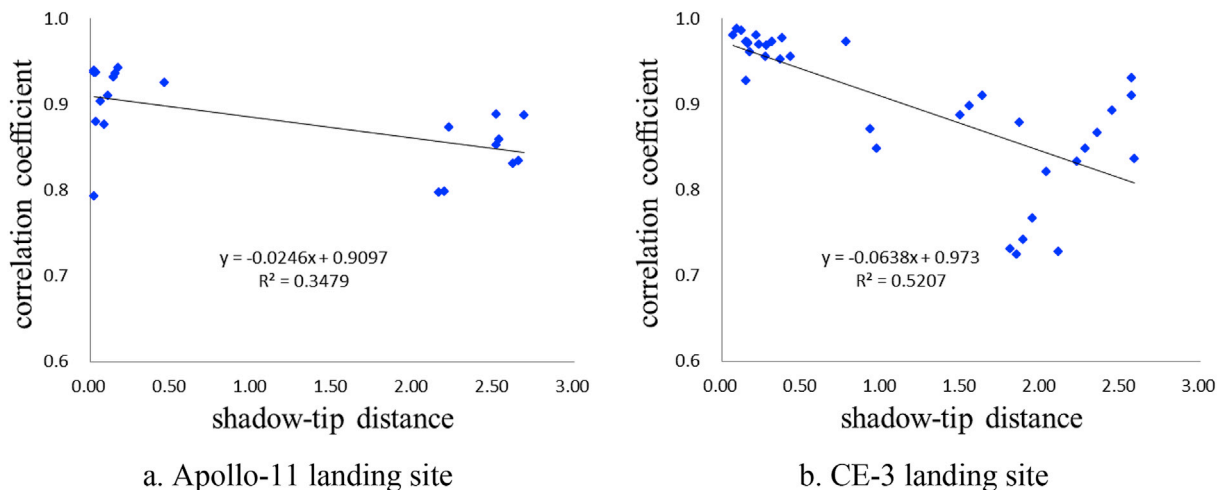


Fig. 4. The relationship between the shadow-tip distance and the correlation coefficient for Apollo-11 (a) and CE-3 (b) landing site.

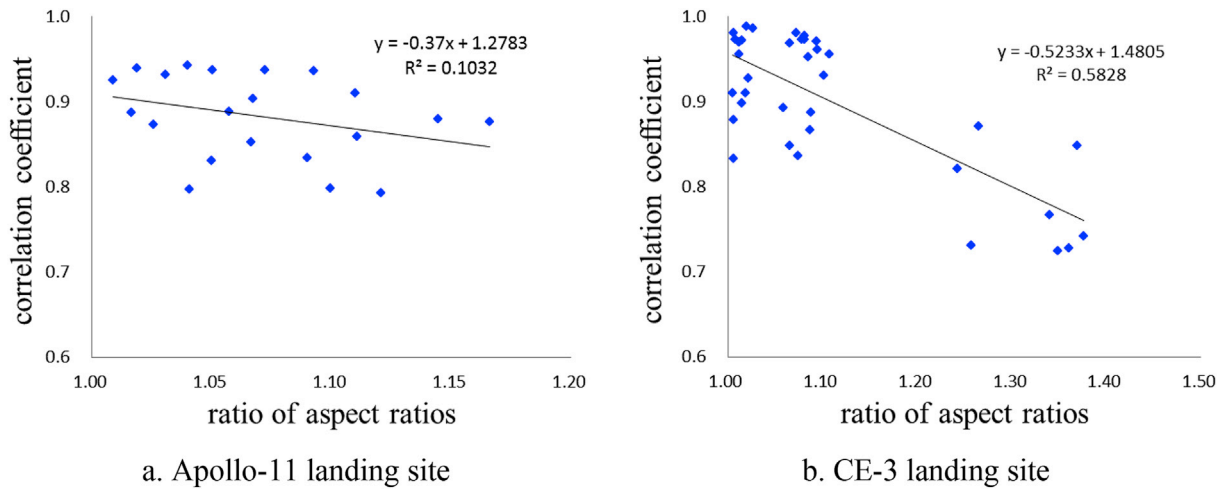


Fig. 5. The relationship between the ratio of aspect ratios and the correlation coefficient for Apollo-11 (a) and CE-3 (b) landing site.

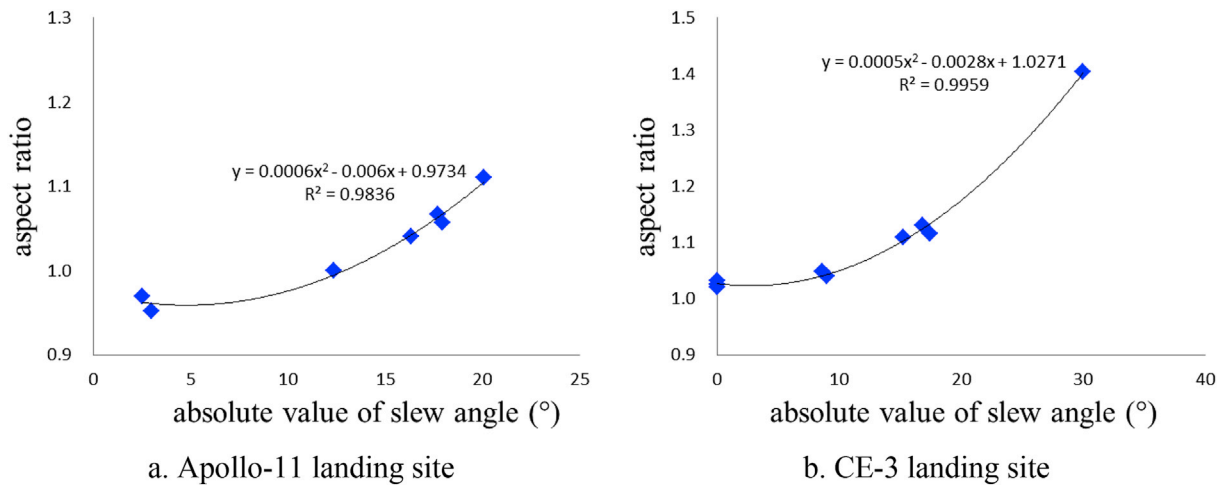


Fig. 6. The relationship between the aspect ratio and absolute value of slew angle for Apollo-11 (a) and CE-3 (b) landing site.

collinearity equation and DEM with an initial height, which is then refined in an iterative way until the difference between the current and previously calculated height coordinate is negligible. Next, with the calculated latitude and longitude coordinates, the grayscale values of each pixel can be obtained from the DOM. We utilize a single DOM to generate both images because examination reveals substantial positional offsets, up to two pixels, between the two orthoimages of the reference pair. However, there is a valid concern that matching the same orthoimage against itself may lead to over-optimistic estimate of match quality when the convergence angle becomes small. Therefore, we experimented with adding some Gaussian white noise with the mean of 0 and variance of 5 gray scales to the DOM when generating the right images of the stereo pairs. As a result, simulated LROC NAC images are generated with each pixel having known ground coordinates. The produced stereo images are totally symmetrical in the cross-track direction under different convergence angle conditions, i.e., the image pair has equal emission angles but on opposite sides of nadir direction. The simulated image pairs are matched by least-squares matching and the matching errors in image space are displayed in Fig. 7.

Fig. 7 reveals that with the increase of convergence angles, the cross-track matching errors increase approximately linearly while the along-track precision has the similar trend but grows very slowly. Referring to the formulas for the standard deviations of the object point from a pair

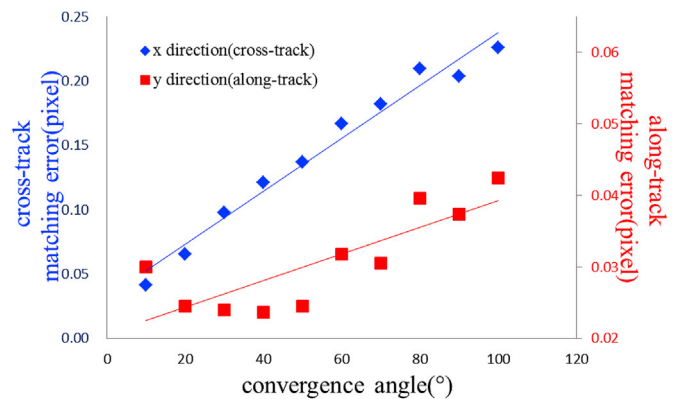


Fig. 7. The relationship between convergence angle and image matching error.

of convergence images as shown in Fig. 8 (Wang, 1990), when assuming  $\alpha = \alpha' = \theta = \theta'$  and keeping  $H$  to be constant, the image measurement errors (image matching errors) can be propagated to object space by the following equations:

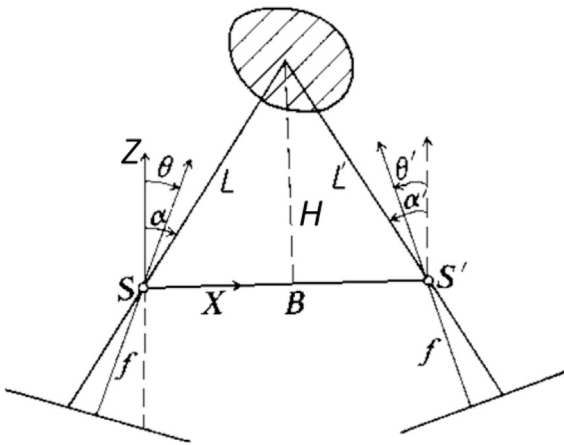


Fig. 8. The intersection condition of a stereo image pair (Wang, 1990).

$$\begin{aligned} \sigma_x &= \frac{H}{f} (1 + \tan^2 \theta) \sigma_s \\ \sigma_y &= \frac{H}{f} \sec \theta \cdot \sigma_s \\ \sigma_z &= \frac{\sqrt{2}H^2}{Bf} (1 + \tan^2 \theta) \sigma_s \\ \sigma_T &= \sqrt{\sigma_x^2 + \sigma_y^2 + \sigma_z^2} \end{aligned} \quad (15)$$

where  $H$  is the LRO flight height,  $\theta$  is the looking angle, assumed to be half the convergence angle here,  $B$  is the baseline length,  $\sigma_x$ ,  $\sigma_y$  are the image measurement errors,  $\sigma_x$ ,  $\sigma_y$ ,  $\sigma_z$  are the geopositioning errors in cross-track, along-track and height directions, respectively, and  $\sigma_T$  is the overall positional error.

Based on Eq. (15), the matching errors in image space depicted in Fig. 7 can be transformed to object space as shown in Fig. 9. The results without considering the image matching errors are shown with the symbol “V” and the others are with “o”. The solid symbols represent the errors in height direction (Z error) and the hollow ones are the overall positional errors. The height errors decrease as a power function as the convergence angles increase while the overall errors decrease and then increase with the turning points located between  $50^\circ$  and  $60^\circ$ . When image matching errors are involved, based on the above simulation results, all errors increase more or less and the turning point of the positional errors moves slightly to a smaller convergence angle, which, to some degree, can explain our experimental results and have important guiding significance in optimal stereo pair selection.

In previous theoretical or simulation research, the image measurement errors are usually taken as constants (e.g., image matching error of half pixel or one-third pixel) without considering the influence of convergence angle. In the above experiment, the image matching error is considered using the linear fitting function from the simulation results, which can give a more realistic result for the geopositioning error. In the future, if a theoretical relationship between image matching error and convergence angle can be derived, the geopositioning precision formula (Eq. (15)) can be updated by replacing the image measurement error with a function of the convergence angle.

### 3.5. Geopositioning precision of multiple images

The geopositioning precision investigations of multi-images are carried out through a progressive strategy and the images of the Apollo-11 landing site are tested thoroughly for their higher resolution. To begin with, the image pair with the highest precision from Section 3.2 is selected and the other five images are added to the pair, in turn, to form

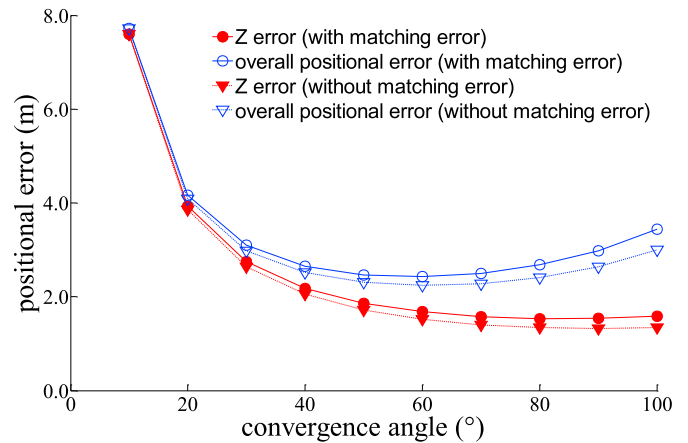


Fig. 9. The relationship between convergence angle and geopositioning error with and without considering image matching error.

3-image stereos. The geopositioning precision is evaluated by check points and the group with the minimum error is chosen for the next step, in which the other four images are added, in turn, to form 4-image stereos. The process repeats until the 7-image 3D triangulation is reached.

In Table 4, the precision reaches 0.43 m, 0.18 m, and 0.39 m in latitude, longitude, and height directions, respectively, when all seven images are combined, which, though not the best, is higher than all of the dual-image and most of the multi-image combinations. In Fig. 10a, the height precision reaches the best condition when three images are involved, while the horizontal precision is best with six images included, which leads to the consequence that the overall precision is optimal when using three images but the precision of three to six images is similar.

To verify the effectiveness of our progressive selection method, the Apollo-11 research is extended to test the use of different numbers of images in all combinations. This means that there are 21 combinations for two and five images, 35 combinations for three and four images, seven combinations for six images, and one combination for all seven images. The optimal and suboptimal triangulation results are listed in Table 5 and the best precision combinations chosen by the above progressive strategy are highlighted.

The entire 21 groups for 2 images have been processed in the abovementioned investigation, which finds that the best combination is A3/A4. As for 3 images, our progressive method chooses A345 as the optimal group and additional experiments show that it remains one of the optimal choices with the other one being the A245 combination, both of which have overall errors of 0.53 m. Further analysis indicates that A4/A5 has the best vertical precision while A2/A4 and A2/A5 surpass most dual-image combinations in horizontal precision, so that A245 has excellent overall precision. In other words, A4/A5 has the largest correlation coefficient in the neighboring range, hence, the best height precision, but its planar precision is relatively low; with the A2 image added, the general geopositioning result reaches the best condition in all tri-image combinations. On the other hand, the A3/A4 has the least total error with its suboptimally even horizontal and vertical precisions. Therefore, based on the A3/A4, the group of A345 will be chosen as the best.

When 4 images are involved, the A1345 (or A3451) is selected as the best combination with a general precision of 0.54 m. The A2345, with a precision of 0.56 m, becomes the suboptimal. In 5-image experiments, the least error combinations are A12456 and A13456 (or A34516), and both have errors of 0.54 m, the latter of which is the chosen result of our progressive method. As for 6 images, the best overall precision combination, A123456 is also the one determined by our progressive method with the second one being A134567.

The above results reveal that with all combinations tested in Apollo-11 experiment, the best geopositioning precision is achieved when 3

**Table 4**

Precisions of best combinations of images in the Apollo-11 experiment. (A3/A4 is the combination ID of A3 and A4 images. In the combination IDs of 3 or more images, the slash and additional A are omitted for simplicity.)

Images added	Number of images	Combination ID	Along-track precision (m)	Cross-track precision (m)	Height precision (m)	Overall precision (m)
M1114021499R +M1126972080L	2	A3/A4	0.39	0.15	0.56	0.70
+M1126986303R	3	A345	0.37	0.07	0.37	0.53
+M1114007294R	4	A3451	0.35	0.10	0.40	0.54
+M1129340193R	5	A34516	0.35	0.14	0.40	0.54
+M1114014396R	6	A345162	0.33	0.15	0.40	0.54
+M1159956344R	7	A3451627	0.43	0.18	0.39	0.61

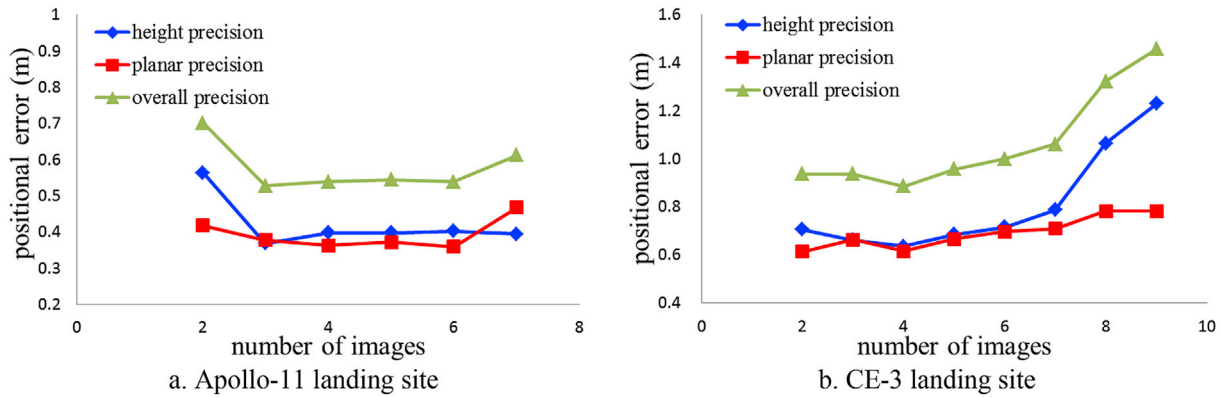


**Fig. 10.** The relationship between the image numbers and the geopositioning precision in object space.

**Table 5**

The optimal and suboptimal results of different image-number groups in the Apollo-11 experiment. The highlighted ones are the combinations chosen by our progressive method. (A345 is the combination ID of A3, A4 and A5 images, similarly hereinafter.)

Number of images	Combination ID	Along-track precision(m)	Cross-track precision(m)	Height precision(m)	Overall precision(m)
3	<b>A345</b>	<b>0.38</b>	<b>0.37</b>	<b>0.37</b>	<b>0.53</b>
	A245	0.37	0.36	0.38	0.53
4	<b>A1345</b>	<b>0.35</b>	<b>0.10</b>	<b>0.40</b>	<b>0.54</b>
	A2345	0.35	0.08	0.44	0.56
5	<b>A13456</b>	<b>0.35</b>	<b>0.14</b>	<b>0.40</b>	<b>0.54</b>
	A12456	0.31	0.15	0.41	0.54
6	<b>A123456</b>	<b>0.33</b>	<b>0.15</b>	<b>0.40</b>	<b>0.54</b>
	A134567	0.44	0.17	0.39	0.61

images are used. Furthermore, the best precision combinations chosen by our proposed method in every image-number group surpass others except in the case of a few same precision results. Therefore, our progressive selection method in the multi-coverage region is proven effective.

Actually in practical application, it is unnecessary to add all the images, and the progressive selection process can stop just when the current positional error with one more images added is larger than the former error. To further illuminate such point, the images of the CE-3 landing site are also tested and when using all nine images for 3D triangulation, the precision is 0.50 m, 0.60 m, 1.23 m in along-track, cross-track, and

height directions, respectively. The results are similar to the Apollo-11 research that the geopositioning precision with nine images is better than most combinations of two or more images. However, when fewer images are selected, the precision can be better than using all 9 images. Fig. 10b displays the relationship between the 3D precision and the number of images used for the CE-3 research. The errors in the horizontal direction do not change very much as more images are added for 3D triangulation, while the vertical errors decrease, then increase from slowly to sharply, with the turning point at four images, which has the precision of 0.50 m, 0.36 m, and 0.64 m. The detailed information is

**Table 6**

The precision of best combinations in different image-number groups in the CE-3 experiment. (C5/C7 is the combination ID of C5 and C7 images. In the combination IDs of 3 or more images, the slash and additional C are omitted for simplicity.)

Images added	Number of images	Combination ID	Along-track precision (m)	Cross-track precision (m)	Height precision (m)	Overall precision (m)
M1144922100L +M1144936321L	2	C5/C7	0.47	0.40	0.71	0.94
+M1144929211L	3	C576	0.54	0.38	0.66	0.94
+M183661683L	4	C5762	0.50	0.36	0.64	0.89
+M1144943432L	5	C57628	0.48	0.46	0.69	0.96
+M181302794L	6	C576281	0.45	0.54	0.72	1.00
+M1144950543L	7	C5762819	0.46	0.54	0.79	1.06
+M1142568554L	8	C57628194	0.50	0.60	1.06	1.32
+M1142554338L	9	C576281943	0.50	0.60	1.23	1.46

summarized in Table 6. The progressive selection process stops at 5-image combination and determines the optimal combination to be the 4-image combination C5762.

To sum up, our progressive method of choosing the best precision image combination can be described as follows. All the dual-image combinations are block adjusted first to get a least error image pair, based on which other remaining images are added to form tri-image stereo, and the precision is evaluated by check points to locate the next best precision combination. If the current best has a larger error than the former one, the final optimal combination will be the former one. Otherwise, the selection process continues until the satisfaction of above requirement.

#### 4. Conclusions

The geopositioning precision of multiple image triangulation is studied in this paper by using seven LROC NAC images of about 1.0 m pixel scale of the Apollo-11 landing site and nine images of about 1.5 m pixel scale of the CE-3 landing site. The experimental results demonstrate that the plane coordinates can achieve a precision of 0.36 m–2.27 m, with a height precision of 0.37 m–7.22 m for the Apollo-11 landing site and a precision of 0.54 m–2.54 m, with a height precision of 0.71 m–8.16 m for the CE-3 landing site, when only two images are used for three-dimensional triangulation. The precisions of using all the images are 0.43 m, 0.18 m, 0.39 m for Apollo-11 and 0.50 m, 0.60 m, 1.23 m for CE-3 landing site in the along-track, cross-track, and height directions, while triangulations with three particularly chosen images for Apollo-11 and four images for CE-3 produce the best precision in this study.

The following conclusions can be drawn from our experimental results.

- 1) We find that with the increase of the convergence angle of a stereo pair, the height error decreases in a power function law, and the overall error decreases and then increases with the turning point located between  $50^\circ$  and  $60^\circ$ . We also find that the image matching error of a stereo pair increases linearly with the increase of convergence angle. Therefore, we recommend the convergence angle should be considered not only as a geometric strength factor, but also as a factor which has effect on the precision of image matching.
- 2) The geopositioning precision is mainly controlled by the convergence angle when it is less than about  $10^\circ$  while the image matching error plays a more critical role when the convergence angle is greater than  $10^\circ$ . This conclusion is meaningful for selection of the best precision stereo pairs from existing data, and for future stereo image acquisition by LROC NAC as well as other orbital imagers. To be specific, based on our experiment results, we recommend that the convergence angle should be the first consideration when getting stereo images and it is better to be larger than  $10^\circ$  but too large (empirically larger than  $40^\circ$ ) is not necessary.
- 3) The shadow-tip distance and aspect ratio are also roughly linear with image matching precision. So they are also important factors which can decide the image pairs selection. In addition to convergence angle, the illumination and aspect ratio are also important when dealing with multi-image triangulation.
- 4) Multi-image triangulation precision is higher than almost all of the dual-image results based on the RFM plus affine model used in this research, demonstrating the advantages of 3D geopositioning with more than two images.
- 5) Triangulation of selected fewer images can produce better precision than using all the images. The proposed progressive image selection method, which can find the best precision combination conveniently, proves to be effective.

Selection of the best image combination for multiple image triangulation is an important issue in planetary photogrammetry. In the future, further studies will be conducted, including theoretical deduction of the

relationship between image matching error and convergence angle for different terrain conditions, triangulation with images of large resolution differences, weighted multiple image triangulation, etc. While we investigated multi-image triangulation precision for relative positioning in this paper, the absolute accuracy of the resultant coordinates remains to be discussed in the future. The absolute accuracy of multi-image triangulation will be evaluated using absolute ground truths, i.e., the coordinates of lunar laser ranging retro reflectors.

#### Acknowledgments

This study was supported in part by National Natural Science Foundation of China (Grant No. 41590851, 41301528 and 41671458). We would like to thank the LROC team (NASA/GSFC/Arizona State University) for making the LROC NAC images available online. J. Oberst gratefully acknowledges being hosted by MIIGAIK and supported by the Russian Science Foundation under project 14-22-00197. We are also grateful to the reviewers for their careful proofreading and insightful comments.

#### Appendix A. Supplementary data

Supplementary data related to this article can be found at <http://dx.doi.org/10.1016/j.pss.2017.07.016>.

#### References

- Bart, G.D., Nickerson, R.D., Lawder, M.T., Melosh, H.J., 2011. Global survey of lunar regolith depths from LROC images. *Icarus* 215 (2), 485–490. <http://dx.doi.org/10.1016/j.icarus.2011.07.017>.
- Becker, K.J., Archinal, B.A., Hare, T.H., Kirk, R.L., Howington-Kraus, E., Robinson, M.S., Rosiek, M.R., 2015. Criteria for automated identification of stereo image pairs. In: *Lunar and Planetary Science Conference, Texas, USA, vol. 46, p. 2703*.
- Clegg-Watkins, R.N., Jolliff, B.L., Boyd, A., Robinson, M.S., Wagner, R., Stopar, J.D., Plescia, J.B., Speyerer, E.J., 2016. Photometric characterization of the Chang'e-3 landing site using LROC NAC images. *Icarus* 273, 84–95. <http://dx.doi.org/10.1016/j.icarus.2015.12.010>.
- Di, K.C., Xu, B., Liu, B., Jia, M.N., Liu, Z.Q., 2016a. Geopositioning precision analysis of multiple image triangulation using LRO NAC lunar images. In: *International Archives of the Photogrammetry, Remote Sensing and Spatial Information Sciences, XXIII ISPRS Congress, Prague, Czech Republic, Vol. XLI-B4*.
- Di, K.C., Ma, R.J., Li, R.X., 2003. Rational functions and potential for rigorous sensor model recovery. *Photogramm. Eng. Remote Sens.* 69 (1), 33–41. <http://dx.doi.org/10.14358/PERS.69.1.33>.
- Di, K.C., Sun, S.J., Yue, Z.Y., Liu, B., 2016b. Lunar regolith thickness determination from 3D morphology of small fresh craters. *Icarus* 267, 12–23. <http://dx.doi.org/10.1016/j.icarus.2015.12.013>.
- Di, K.C., Liu, Y.L., Liu, B., Peng, M., Hu, W.M., 2014. A Self-calibration bundle adjustment method for photogrammetric processing of Chang'E-2 stereo lunar imagery. *IEEE Trans. Geosci. Remote Sens.* 52 (9), 5432–5442.
- Haase, I., Oberst, J., Scholten, F., Wählisch, M., Gläser, P., Karachetseva, I., Robinson, M.S., 2012. Mapping the Apollo 17 landing site area based on Lunar Reconnaissance Orbiter Camera images and Apollo surface photography. *J. Geophys. Res. Planets* 117 (E12).
- Henriksen, M.R., Manheim, M.R., Speyerer, E.J., Robinson, M.S., LROC Team, 2016. Extracting accurate and precise topography from LROC narrow angle camera stereo observations. In: *The International Archives of the Photogrammetry, Remote Sensing and Spatial Information Sciences, XXIII ISPRS Congress, Prague, Czech Republic, Vol. XLI-B4*.
- Henriksen, M.R., Manheim, M.R., Burns, K.N., Seymour, P., Speyerer, E.J., Deran, A., Boyd, A.K., Howington-Kraus, E., Rosiek, M.R., Archinal, B.A., Robinson, M.S., 2017. Extracting accurate and precise topography from LROC narrow angle camera stereo observations. *Icarus* 283, 122–137. <http://dx.doi.org/10.1016/j.icarus.2016.05.012>.
- Humm, D.C., Tschimmel, M., Brylow, S.M., Mahanti, P., Tran, T.N., Braden, S.E., Wiseman, S., Danton, J., Eliason, E.M., Robinson, M.S., 2016. Flight calibration of the LROC narrow angle camera. *Space Sci. Rev.* 200 (1), 431–473. <http://dx.doi.org/10.1007/s11214-015-0201-8>.
- Jeong, J., Kim, T., 2014. Analysis of dual-sensor stereo geometry and its positioning accuracy. *Photogramm. Eng. Remote Sens.* 80 (7), 653–661.
- Jeong, J., Yang, C., Kim, T., 2015. Geo-positioning accuracy using multiple-satellite images: IKONOS, QuickBird, and KOMPSAT-2 stereo images. *Remote Sens.* 7 (4), 4549–4564.
- Karachetseva, I., Oberst, J., Scholten, F., Konopikhin, A., Shingareva, K., Cherepanova, E., Guskova, E., Haase, I., Peters, O., Plescia, J., Robinson, M., 2013. Cartography of the Lunokhod-1 landing site and traverse from LRO image and stereo-topographic data. *Planet. Space Sci.* 85, 175–187. <http://dx.doi.org/10.1016/j.pss.2013.06.002>.

- Keller, J.W., Petro, N.E., Vondrak, R.R., 2016. The lunar reconnaissance orbiter mission—six years of science and exploration at the Moon. *Icarus* 273, 2–24. <http://dx.doi.org/10.1016/j.icarus.2015.11.024>.
- Kirk, R.L., Archinal, B.A., Gaddis, L.R., Rosiek, M.R., 2012. Lunar cartography: progress in the 2000s and prospects for the 2010s. *Int. Arch. Photogramm. Remote Sens. Spatial Inf. Sci.* B4, 489–494.
- Kirk, R.L., Howington-Kraus, E., Hare, T.M., Jorda, L., 2016. The effect of incidence angle on stereo DTM quality: simulations in support of Europa exploration. In: *The International Archives of the Photogrammetry, Remote Sensing and Spatial Information Sciences, XXIII ISPRS Congress, Prague, Czech Republic, vols. III-4*. <http://dx.doi.org/10.5194/isprs-annals-III-4-103-2016>.
- Liu, B., Liu, Y.L., Di, K.C., Sun, X.L., 2014. Block adjustment of Chang'E-1 images based on rational function model. In: *Remote Sensing of the Environment: 18th National Symposium on Remote Sensing of China. International Society for Optics and Photonics*. <http://dx.doi.org/10.1117/12.2063712>, 91580G-91580G.
- Liu, B., Di, K.C., Wang, B.F., Tang, G.S., Xu, B., Zhang, L.L., Liu, Z.Q., 2015a. Positioning and precision validation of Chang'E-3 Lander based on multiple LRO NAC images (in Chinese). *Chin. Sci. Bull.* 60 (28–29), 2750–2757.
- Liu, B., Xu, B., Di, K.C., Jia, M.N., 2016. A solution to low fitting precision of planetary orbiter images caused by exposure time changing. In: *International Archives of the Photogrammetry, Remote Sensing and Spatial Information Sciences, XXIII ISPRS Congress, Prague, Czech Republic*, pp. 441–448.
- Liu, Z.Q., Di, K.C., Peng, M., Wan, W.H., Liu, B., Li, L.C., Yu, T.Y., Wang, B.F., Zhou, J.L., Chen, H.M., 2015b. High precision landing site mapping and rover localization for Chang'e-3 mission. *Sci. China Phys. Mech. Astronomy* 58 (1), 1–11.
- Mazarico, E., Rowlands, D.D., Neumann, G.A., Smith, D.E., Torrence, M.H., Lemoine, F.G., Zuber, M.T., 2012. Orbit determination of the lunar reconnaissance orbiter. *J. Geodesy* 86 (3), 193–207. <http://dx.doi.org/10.1007/s00190-011-0509-4>.
- NAIF, 2014. Lunar Reconnaissance Orbiter Camera (LROC) Instrument Kernel v18. [http://naif.jpl.nasa.gov/pub/naif/pds/data/lro-l-spice-6-v1.0/lrosp\\_1000](http://naif.jpl.nasa.gov/pub/naif/pds/data/lro-l-spice-6-v1.0/lrosp_1000).
- Robinson, M.S., Brylow, S.M., Tschimmel, M., Humm, D., Lawrence, S.J., Thomas, P.C., Denevi, B.W., Bowman-Cisneros, E., Zerr, J., Ravine, M.A., Caplinger, M.A., Ghaemi, F.T., Schaffner, J.A., Malin, M.C., Mahanti, P., Bartels, A., Anderson, J., Tran, T.N., Eliason, E.M., Mcewen, A.S., Turtle, E., Jolliff, B.L., Hiesinger, H., 2010. Lunar reconnaissance orbiter camera (LROC) instrument overview. *Space Sci. Rev.* 150, 81–124. <http://dx.doi.org/10.1007/s11214-010-9634-2>.
- Speyerer, E.J., Wagner, R.V., Robinson, M.S., Licht, A., Thomas, P.C., Becker, K., Anderson, J., Brylow, S.M., Humm, D.C., Tschimmel, M., 2016. Pre-flight and on-orbit geometric calibration of the lunar reconnaissance orbiter camera. *Space Sci. Rev.* 200 (1–4), 357–392. <http://dx.doi.org/10.1007/s11214-014-0073-3>.
- Tao, C.V., Hu, Y., 2001. A comprehensive study of the rational function model for photogrammetric processing. *Photogrammetric Eng. Remote Sens.* 67 (12), 1347–1357.
- Tran, T., Howington-Kraus, E., Archinal, B., Rosiek, M., Lawrence, S.J., Gengl, H., Nelson, D., Robinson, M.S., Beyer, R., Li, R., Oberst, J., Mattson, S., LROC Science Team, 2010a. Generating digital terrain models from LROC stereo images with SOCET SET. In: *Lunar and Planetary Science Conference, Texas, USA, vol. 41*, p. 2515.
- Tran, T., Rosiek, M.R., Beyer, R.A., Mattson, S., Howington-Kraus, E., Robinson, M.S., Archinal, B.A., Edmundson, K., Harbour, D., Anderson, E., the LROC Science Team, 2010b. Generating digital terrain models using LROC NAC images. In: *ASPRS/CaGIS 2010 Fall Specialty Conference, Orlando, Florida, USA*.
- Wang, J.K., Di, K.C., Li, R., 2005. Evaluation and improvement of geopositioning accuracy of IKONOS stereo imagery. *ASCE J. Surv. Eng.* 131 (2), 35–42.
- Wang, Z.Z., 1990. *Principles of Photogrammetry (With Remote Sensing)*. Press of Wuhan Technical University of Surveying and Mapping and Publishing House of Surveying and Mapping, Beijing, pp. 327–330.
- Wagner, R.V., Nelson, D.M., Plescia, J.B., Robinson, M.S., Speyerer, E.J., Mazarico, E., 2017. Coordinates of anthropogenic features on the Moon. *Icarus* 283, 92–103. <http://dx.doi.org/10.1016/j.icarus.2016.05.011>.
- Wu, B., Li, F., Ye, L., Qiao, S., Huang, J., Wu, X.Y., Zhang, H., 2014. Topographic modeling and analysis of the landing site of Chang'E-3 on the Moon. *Earth Planet. Sci. Lett.* 405, 257–273. <http://dx.doi.org/10.1016/j.epsl.2014.09.009>.